Elasticity mediated yielding of an elasto-viscoplastic fluid in a plane channel flow

Teodor Burghelea, Miguel Moyers-González

Metadata of the article that will be visualized in OnlineFirst

ArticleTitle	Elasticity mediated yielding of an elasto-viscoplastic fluid in a plane channel flow	
Article Sub-Title		
Article CopyRight	The Author(s), under exclusive licence to Springer-Verlag GmbH Germany, part of Springer Nature (This will be the copyright line in the final PDF)	
Journal Name	Theoretical and Computational Fluid Dynamics	
Corresponding Author	FamilyName	**Burghelea**
	Particle	
	Given Name	**Teodor**
	Suffix	
	Division	Laboratoire de Thermique et Énergie de Nantes, LTeN, UMR 6607
	Organization	Nantes Université , CNRS
	Address	Rue Christian Pauc, Nantes, 44306, France
	Phone	
	Fax	
	Email	Teodor.Burghelea@univ-nantes.fr
	URL	
	ORCID	
Author	FamilyName	**Moyers-González**
	Particle	
	Given Name	**Miguel**
	Suffix	
	Division	School of Mathematics and Statistics
	Organization	University of Canterbury
	Address	Private Bag 4800, Christchurch, 8140, New Zealand
	Phone	
	Fax	
	Email	miguel.moyersgonzalez@canterbury.ac.nz
	URL	
	ORCID	
Schedule	Received	7 Jan 2025
	Revised	
	Accepted	17 Sep 2025
Abstract	The study presents a numerical investigation of unsteady plane channel flows of an elasto-viscoplastic material using the Herschel-Bulkley variant of the Saramito elasto-viscoplastic model [1] (SRM-HB), which incorporates both viscoelastic and viscoplastic behaviour. Yield stress fluids exhibit a dual nature, behaving as solids below a critical stress threshold and flowing as non-Newtonian fluids above it. This duality is crucial for numerous industrial applications and remains an area of active research. By examining the unsteady flow dynamics driven by steady and unsteady pressure gradients in a plane channel, this work evaluates the performance of the SRM-HB model against experimental data obtained with Carbopol gels. The findings highlight the significant role of elasticity in the yielding process and the resulting flow characteristics. Various flow scenarios, including creep tests, unsteady pressure ramps, and large-amplitude oscillatory flows, are analyzed to elucidate the complex interplay between elastic and plastic responses. The results demonstrate that the SRM-HB model effectively captures the transient flow behavior and hysteresis phenomena observed experimentally, providing insight into the material's yielding and flow mechanisms.	
Keywords (separated by '-')	Elasto-viscoplastic materials - Saramito model - Unsteady flow - Pipkin space	
Footnote Information		

Theor. Comput. Fluid Dyn. _####################_
https://doi.org/10.1007/s00162-025-00761-1

ORIGINAL ARTICLE

Teodor Burghelea · Miguel Moyers-González

Elasticity mediated yielding of an elasto-viscoplastic fluid in a plane channel flow

Received: 7 January 2025 / Accepted: 17 September 2025

Abstract The study presents a numerical investigation of unsteady plane channel flows of an elasto-viscoplastic material using the Herschel-Bulkley variant of the Saramito elasto-viscoplastic model [1] (SRM-HB), which incorporates both viscoelastic and viscoplastic behaviour. Yield stress fluids exhibit a dual nature, behaving as solids below a critical stress threshold and flowing as non-Newtonian fluids above it. This duality is crucial for numerous industrial applications and remains an area of active research. By examining the unsteady flow dynamics driven by steady and unsteady pressure gradients in a plane channel, this work evaluates the performance of the SRM-HB model against experimental data obtained with Carbopol gels. The findings highlight the significant role of elasticity in the yielding process and the resulting flow characteristics. Various flow scenarios, including creep tests, unsteady pressure ramps, and large-amplitude oscillatory flows, are analyzed to elucidate the complex interplay between elastic and plastic responses. The results demonstrate that the SRM-HB model effectively captures the transient flow behavior and hysteresis phenomena observed experimentally, providing insight into the material's yielding and flow mechanisms.

Keywords Elasto-viscoplastic materials · Saramito model · Unsteady flow · Pipkin space

1 Introduction

Yield stress fluids represent a distinct class of complex fluids that exhibit a dual response when subjected to an external stress: a solid-like behaviour (characterised by deformation but no macroscopic flow) below a critical threshold generally referred to as the *"yield stress"* and a non-Newtonian fluid behavior beyond this threshold. During the past three decades, the interest in yield stress materials has increased steeply and continuously. This is most probably due to an increasing number of practical applications relevant to a variety of industrial sectors (oil field engineering, cosmetics, food industry, polymer processing, pharmaceutical industry etc.) and to a number of intellectual challenges they still pose. Whereas due to significant recent advances in rheometry and the substantially improved accuracy of the modern rheometers the long standing debate related to the existence of a true yield stress behavior initiated by the seminal work of Barnes and Walters [2,3] seems to be now resolved, there currently remain several discussions on the existence of a simple or *"model"* yield stress behavior, [4]. In a nutshell, a simple or *"model"* yield stress behavior is generally understood as a yielding behaviour that may be accurately described by the Herschel-Bulkley constitutive law, $\tau = \tau_y + K\dot{\gamma}^n$. Here

T. Burghelea (✉)
Laboratoire de Thermique et Énergie de Nantes, LTeN, UMR 6607, Nantes Université , CNRS, Rue Christian Pauc, Nantes 44306, France
E-mail: Teodor.Burghelea@univ-nantes.fr

M. Moyers-González
School of Mathematics and Statistics, University of Canterbury, Private Bag 4800, Christchurch 8140, New Zealand
E-mail: miguel.moyersgonzalez@canterbury.ac.nz

τ_y stands for the yield stress, K for the consistency, and n for the power law index. Thus, according to this picture, the solid-fluid transition occurs precisely at the yield point ($\tau = \tau_y$) and the deformation states are fully reversible upon increasing/decreasing stresses. Deviations from this idealized yielding picture mainly originate from three distinct phenomena: elasticity, thixotropy and shear banding. Depending on the physico-chemical nature of the yield stress material, the details of its micro-structure, and the kinematics of the flow one or several of these effects may manifest - often in a coupled manner. Along an experimental line, the existence of a material that fully fits the bill of a *"model"* yield stress fluid made the object of systematic studies, [4,5]. Carbopol gels have been traditionally considered as *"model"* yield stress fluids, [6,7]. Although they do not exhibit noticeable thixotropic effects [8], some flows of Carbopol gels exhibit a number of features that depart from the model behaviour: hysteresis of deformation states in either simple rheometric flows [9,10] or unsteady pipe flows [11], the ability to develop thermo-convective instabilities [12]. As such Carbopol gels are structurally stable over extended periods oftimes and, as already stated above, show no significant thixotropic effects, such behavior can be mostly attributed to the presence of elastic effects that accompany the viscoplastic response around the yield point, [13].

Based on these experimental facts, it is rather clear that a realistic rheological model able to account for such flow behavior should include an elastic part of the stress tensor. An early attempt to combine a Herschel-Bulkley like yielding picture with elastic effects modeled simplistically by a Maxwell like picture was made by Putz and coworkers, [9,14]. This model was initially formulated in a scalar form with the initial purpose of describing the hysteresis observed during controlled stress loading/unloading ramps performed with Carbopol gels.

In [15] the authors studied numerically the Poiseuille flow of an elastoviscoplastic fluid, focusing on how different slip conditions at the wall affect flow behaviour. Using the rheological model by Putz and Burghelea [9], the authors simulate the flow driven by a time-dependent pressure ramp and analyse how various slip laws influence the average velocity across the pipe. The study focuses on the role that slip at the wall can have in the transition from solid to fluid states. The slip condition determines how the material transitions between behaving as a solid under low stress and flowing as a fluid when stress exceeds the yield point. It is found that the solid-fluid transition is highly sensitive to the slip-law used. Different slip laws shift the solid-fluid transition region, impacting when and how the material begins to flow. Interestingly, the simulations showed that the microstructure function remains unchanged for all slip-laws tested. This lead the authors to conclude that the rheological model predicts that stresses and deformation rates remain the same irrespectively of the boundary conditions at the wall, i.e., stresses and deformation rates are governed by the bulk rheological constitutive relation. Therefore, if time-dependent effects are introduced by what happens at the walls, one should think carefully about how to connect slip-law and constitutive equations.

In the present work, we are mainly interested in the yielding behaviour of an elastoviscoplastic material in a simple flow configuration. In order to choose the "best" rheological model, we look at the works of Fraggedakis et al. [16]. In their work, the authors present a comparison of five elasto-visco-plastic (EVP) fluid models within the framework of rheometric flows and complex flow scenarios, such as a spherical particle falling under gravity. The study evaluates models based on their ability to predict the behaviour of EVP fluids, highlighting the differences in predictions and limitations, especially under non-homogeneous and oscillatory flow conditions. The Saramito [17] (SRM) model and its Herschel-Bulkley variant [1] (SRM-HB) , Park and Liu [18], (PL) model, and Belblidia et al. [19], (BWW) model are tested, with the SRM outperforming the other two models.

The SRM model has been employed in numerical simulations of flows of elasto-viscoplastic fluids for a number of rather sophisticated and technically challenging configurations including sedimentation of solid bodies [20], buoyancy driven motion of single or multiple bubbles [21,22] and, more recently, porous media [23]. Each of these numerical results clearly advocates for an important role of elasticity in the dynamics.

Quite surprisingly perhaps, a flow setting that is kinematically much simpler than those exemplified above such as an unsteady channel flow has received significantly less attention. In spite of its simplicity, this flow setting is relevant to a number of industrial problems related to oil field engineering (startup of crude oils in long pipes) and polymer processing. From a more fundamental perspective, studying transient flows of elasto-viscoplastic fluids driven by steady and unsteady pressure gradients in plane channels offers practical means of assessing the performance of the SRM-HB model by direct comparison with existing experimental results obtained with a Carbopol gel, [11].

We feel that a bridge between viscometric flows and the more complex flow problems (sedimentation, flows in porous media etc.) is a basic pipe flow. As already mentioned, this flow configuration is widely used in

industry applications. Hence, studying how a constitutive model performs under these conditions is a worthy validation test.

2 Problem description, numerical method

2.1 Governing equations

We study flows of an elasto-viscoplastic material in a plain channel of length $L = 1$ and width $W = 1$. We conside flows driven by a pressure drop ΔP which can be either steady (i.e. creep flows) or unsteady (pressure ramps, oscillatory flows) and monitor the transient flow response. The flow is governed by the continuity and momentum conservation:

$$\rho\left(\frac{\partial \boldsymbol{u}}{\partial t} + \boldsymbol{\nabla}\left(\boldsymbol{u}\cdot\boldsymbol{u}\right)\right) = -\nabla P + \nabla\cdot\boldsymbol{\tau} \tag{1}$$

$$\nabla\cdot\boldsymbol{u} = 0 \tag{2}$$

Here ρ stands for the density of the fluid, $\boldsymbol{u}$ for its velocity, P for the driving pressure gradient and $\boldsymbol{\tau}$ for the stress tensor. Eqs. 1 are complemented by non-slip boundary conditions. The stress tensor may be written as a sum of the solvent contribution $\boldsymbol{\tau_s}$ and the polymeric contribution $\boldsymbol{\tau_p}$, $\boldsymbol{\tau} = \boldsymbol{\tau_s} + \boldsymbol{\tau_p}$. The solvent contribution behaves in a Newtonian manner, $\boldsymbol{\tau_s} = 2\eta_s\boldsymbol{D}$ where η_s is the solvent viscosity and $\boldsymbol{D} = \frac{1}{2}\left[\boldsymbol{\nabla u} + \boldsymbol{\nabla u}^T\right]$ is the rate of strain tensor. Through the computations reported herein, $\eta_s = 1$. The polymeric part of the stress tensor $\boldsymbol{\tau}_p$ describes the elasto-viscoplastic effects which emerge from the microstructure of the material. For viscoelastic liquids the polymer part of the stress tensor is often written $\boldsymbol{\tau}_p = \frac{\eta_p}{\lambda} f\left(\boldsymbol{A}\right)$ where λ is the polymer relaxation time, η_p the plastic viscosity and f a function of the conformation tensor $\boldsymbol{A}$, [24]. We consider $f\left(\boldsymbol{A}\right) = \boldsymbol{A} - \boldsymbol{I}$ and assume a linear relaxation law for the conformation tensor, $\overset{\triangledown}{\boldsymbol{A}} = -\frac{1}{\lambda}\left(\boldsymbol{A} - \boldsymbol{I}\right)$. Here $\overset{\triangledown}{(.)}$ stands for the upper convective time derivative. The idea of combining viscoelastic and viscoplastic effects originates from Saramito [1,17] and consists of introducing a critical stress τ_y at which the rheological response of the material switches from a solid behavior to a liquid one. The Herschel-Bulkley variant of the SRM model [1] combines a Herschel-Bulkley model and an Oldroyd-B one:

$$\frac{1}{G}\overset{\triangledown}{\boldsymbol{\tau}}_p + S\left(\boldsymbol{\tau_p}, \tau_y\right)\boldsymbol{\tau}_p - 2\boldsymbol{D} = 0 \tag{3}$$

where G is the elastic modulus. The convective derivative of the polymeric stress is defined by

$$\overset{\triangledown}{\boldsymbol{\tau}}_p = \frac{\partial \boldsymbol{\tau_p}}{\partial t} + \left(\boldsymbol{u}\cdot\nabla\right)\boldsymbol{\tau_p} - \left(\nabla\boldsymbol{u}\right)\boldsymbol{\tau_p} - \boldsymbol{\tau_p}\left(\nabla\boldsymbol{u}\right)^T \tag{4}$$

For most of the computations (the exceptions are specifically discussed through the text) the elastic modulus was fixed, $G = 1$. The switch function is defined by

$$S\left(\boldsymbol{\tau_p}, \tau_y\right) = \max\left(0, \frac{|\boldsymbol{\tau_p^d}| - \tau_y}{K|\boldsymbol{\tau_p^d}|^n}\right)^{1/n} \tag{5}$$

where K is the consistency, n the power law index, $\boldsymbol{\tau_p^d} = \boldsymbol{\tau_p} - \frac{Trace(\boldsymbol{\tau_p})}{2}\boldsymbol{I}$ the deviatoric part of the polymeric stress and $|\boldsymbol{\tau_p^d}| = \sqrt{1/2\boldsymbol{\tau_p^d}\cdot\boldsymbol{\tau_p^d}}$. Through all the computations reported herein we have used $K = 1, n = 0.5$.

In the regions of the flow where $|\boldsymbol{\tau_p^d}| > \tau_y$ the material behaves as a fluid or is yielded while otherwise behaves as a solid or is unyielded.

The relevant non-dimensional numbers governing the elasto-viscoplastic flow are the Weissenberg number $Wi = \frac{1}{SG}\dot{\gamma}$, the Bingham number $Bn = \frac{\tau_y}{\eta\dot{\gamma}}$ and the Reynolds number $Re = \frac{\rho U^2}{\tau_y + K\left(\frac{2U}{W}\right)^n}$. Here U is a velocity scale and $\dot{\gamma}$ is the rate of shear which, according to [25], may be understood as the second invariant of the rate of strain tensor $\dot{\gamma} = \sqrt{1/2\boldsymbol{D}:\boldsymbol{D}}$. As the flows we focus on are pressure driven, we estimate the Bingham number via the scale of the imposed pressure drop, $Bn = \frac{2L\tau_y}{W\Delta P}$. The maximum value of the Reynolds number explored was $Re^{max} = 0.3$ so the flows are always laminar.

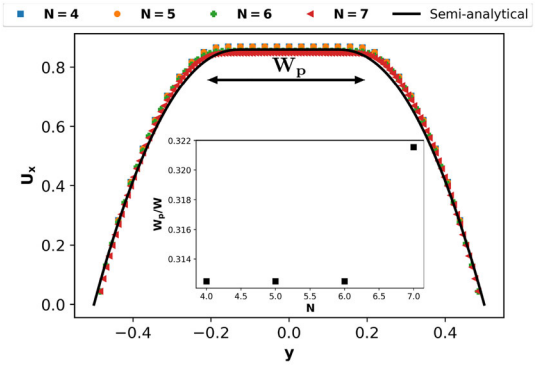

(a)

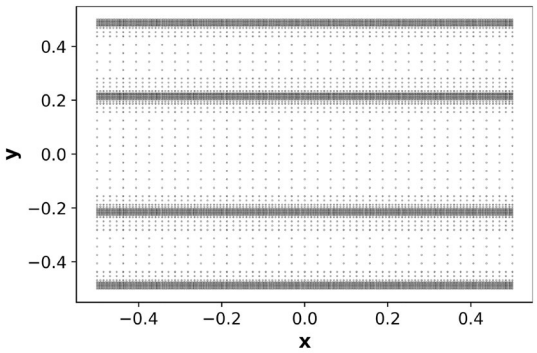

(b)

Fig. 1 (a) Transverse profiles of the axial velocity computed for three distinct grid levels $\Delta y = 1/2^N$: squares - $N = 4$, circles - $N = 5$, pluses - $N = 6$, triangles - $N = 7$. The full line is the semi-analytical solution (see appendix A). The dependence of the plug width on the level of grid refinement is shown in the inset. (b) Example of adaptive mesh

2.2 Numerical method

To solve numerically the flow problem described above, we use the open source code Basilisk-C, [26].

Basilisk contains a well benchmarked implementation of the Oldroyd-B model for solving viscoelastic flows for a given relaxation time λ and polymeric contribution to the viscosity η_p [27]. To accurately resolve the solid-fluid interfaces and the velocity boundary layer, an adaptive quad-tree mesh refinement based on a wavelet algorithm was used, Fig. 1(b).

To check for grid convergence and to validate our code, simulations of a steady flow driven by an imposed pressure drop $\Delta P = 10$ were performed for four distinct sizes of the base grid $\delta y = 1/2^N$ with $N = 4, 5, 6, 7$. The transversal profiles of the axial velocity computed at the exit of the flow channel for each level of refinement of the base grid are presented in Fig. 1(a). Upon a quick visual inspection of the four distinct sets of results no substantial differences can be noted. Also, the computed velocity profiles overlap fairly well with the semi-analytical solution derived in the appendix A. The plug width obtained from each run is shown in the main inset. The average plug size over these four individual tests is $W_p^{av} = 0.3147$ and the standard deviation is $W_p^{std} = 0.00392$, accounting for roughly 1.2% of the mean value. The grid independence test discussed above refers to a steady state flow case. Additional grid independence results for a unsteady flow case are presented in the appendix C.

Through the rest of the simulations reported herein, we use an adaptive grid with $N = 5$ as a level of refinement of the base grid.

The maximal time step used through the simulations reported herein was $DT = 10^{-5}$. The indepence of the results on the choice of the maximal time step is discussed in appendix B.

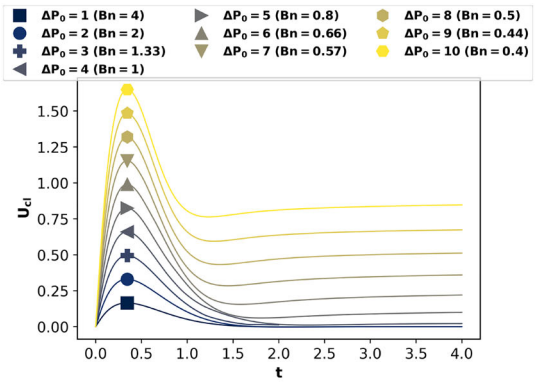

(a)

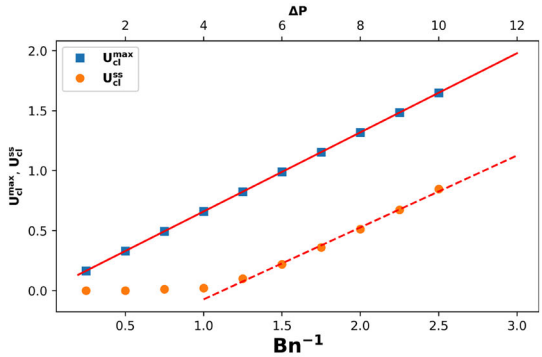

(b)

Fig. 2 (a) Time series of the centre line velocity U_{cl} for various values of the imposed pressure drop ΔP_0 indicated in the insert. (b) Dependence of the maximum centre line speed U_{cl}^{max} (squares) and of the steady state speed U_{cl}^{ss} on imposed pressure drop ΔP_0. The lines are linear fitting functions (see text for discussion)

3 Results

3.1 Creep tests

One of the simplest, yet very insightful flows that one can investigate is a transient creep flow driven by a constant imposed pressure drop ΔP_0. Of particular interest in this context would be to understand the combined role of elastic and plastic behaviors in the transient dynamics of the flow.

The time series of the velocity of the center line U_{cl} obtained for several values of the imposed pressure drop P_0 is illustrated in Fig. 2(a). Regardless of the magnitude of the imposed pressure drop, the time series of the center line velocity exhibits an overshoot behavior corresponding to $t_{max} = 0.344$. This observation is qualitatively similar to the overshoot behavior observed during creep tests performed with Carbopol gels in rheometric geometries, [13]. For pressures imposed smaller than a critical value $\Delta P_c = 4$ which corresponds to a critical Bingham number $Bn_c = 1$, the center line velocity further decays to zero and no permanent flow is established. For imposed pressure drops larger than this critical value, a permanent flow with a centerline speed U_{cl}^{ss} is established. Regardless of the value of the imposed pressure drop, the time series of the center line velocity exhibit an overshoot prior to reaching a steady state. The overshoot speed U_{cl}^{max} scales linearly with the inverse Bingham number (the squares and the full line in Fig. 2(b)), $U_{cl}^{max} = 0.659 Bn^{-1}$. Past the critical pressure $\Delta P_c = 4$ ($Bn_c = 1$), the steady-state center-line speed also scales linearly with the inverse Bingham number, $U_{ss} = -0.67 + 0.6 Bn^{-1}$. The emergence of overshoot effect is of a purely elastic nature. Thus, by gradually diminishing the elastic effects (by increasing G), the magnitude of the overshoot effect decreases monotonically (data not show here).

More insights into the overshoot behavior may be obtained by analyzing several flow profiles before and after the overshoot is observed, Fig. 3.

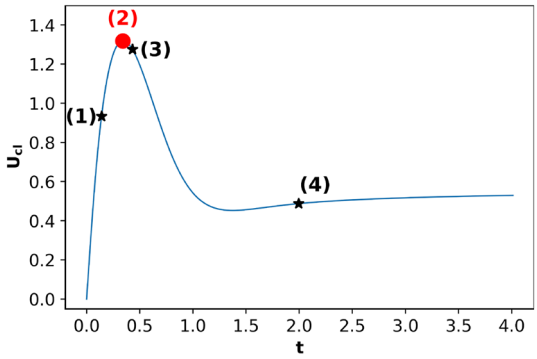

(a)

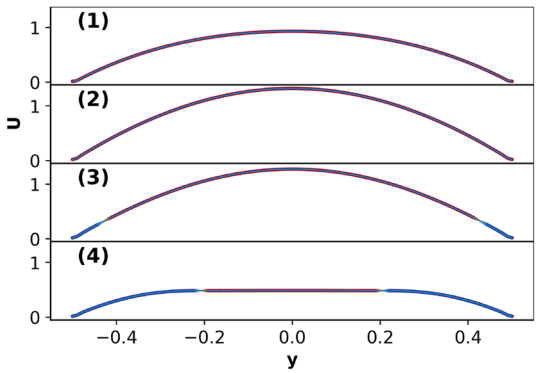

(b)

Fig. 3 (a) Overshoot behavior observed for a constant imposed pressure drop $P_0 = 8$. (b) Transverse profiles of the axial velocity corresponding to the transient states labelled in panel (a). The color (blue/red) codes the yielded/unyielded flow regions

We have chosen for illustration the case $\Delta P_0 = 8$ which is larger than the critical yielding pressure ΔP_c, allowing a permanent steady-state flow to be observed and focus on four distinct time instants labeled in Fig. 3(a). Corresponding to each state (time instant) labeled in Fig. 3(a) we plot in Fig. 3(b) the transverse profile of the axial velocity color-coded to highlight the yielded/unyielded regions in blue/red. Prior to the overshoot, $t < t_0 = 0.34$, the material is unyielded over the entire width of the channel, panel (1) in Fig. 3(b). When the overshoot is observed at $t = t_0$, the material is still fully un-yielded (panel (2)) but starts to gradually yield near the boundaries right after the overshoot, panel (3). At this early stage of the yielding process the velocity profile in the central un-yielded part is not flat which is consistent with a elastic deformation of the solid part. A flat central un-yielded plug forms when a steady state of the axial speed is observed, panel (4). Right after the overshoot, the material starts to yield gradually from the channel's boundaries (panel (3)) and a flat central plug consistent with a Herschel-Bulkley behavior develops when a steady state is reached (panel (3)).

3.2 Unsteady pressure ramps

We focus in the following on the response to linear increasing/decreasing ramps in the imposed pressure drop, Fig. 4(a), defined as:

$$\Delta P(t) = \Delta P_{max} \frac{-N + \sum_{k=0}^{N-1} H(t - kt_0) + \sum_{k=N}^{2N-1} H(kt_0 - t)}{N} \tag{6}$$

Here H stands for the Heaviside step function, t_0 is the duration of each step of the ramp $\Delta P_{max} = 10$ is the maximal value of the imposed pressure drop and $T_{max} = N\, t_0$ is the total duration of the loading/unloading branches of the ramp. For all the simulation to be further discussed, we have used $N = 20$ steps for each branch of the ramp. Such increasing/decreasing controlled pressure ramp is precisely the same type of unsteady flow

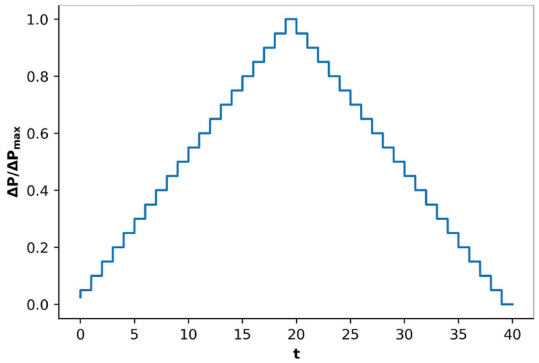

(a)

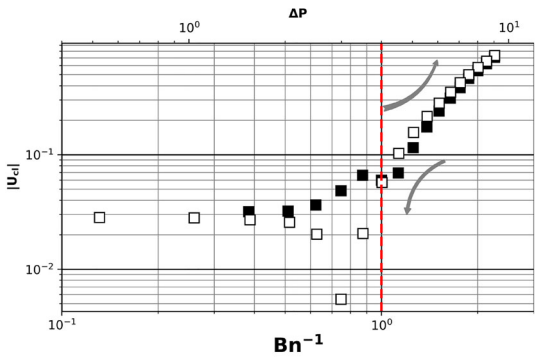

(b)

Fig. 4 (a) Example of the imposed pressure drop ramp. The time per step is $t_0 = 0.2$ and the maximal imposed pressured drop is $\Delta P_{max} = 10$ (b) Centre line velocity U_{cl} computed during a pressure ramp. The full/empty symbols refer to the increasing/decreasing branches of the ramp. The time per step was $t_0 = 0.5$. The vertical dashed line indicates the critical Bingham number, $Bn_c = 1$

that has been studied experimentally in Ref. [11]. As the maximal pressure has been chosen $\Delta P_{max} > \Delta P_c = 4$ corresponding to the yielding of the material (see Fig. 2) the loading/unloading sequence will first yield then un-yield the material. The dependence of the absolute value of the center-line velocity $|U_{cl}|$ measured at the channel exit on the inverse Bingham number is presented in Fig. 4(b). The flow states observed upon increasing/decreasing pressure drops are reversible only for imposed pressures larger than the critical value $\Delta P_c = 4$ ($Bn_c = 1$). The hysteresis behavior observed in Fig. 4(b) is fully consistent with the experimental observations performed using a Carbopol gel in a unsteady pipe flow, [11], and with rheological measurements, [9,13]. Just as observed through the experiments performed with a Carbopol gel, the cusp visible on the decreasing branch of the controlled pressure drop ramp (the empty symbols in Fig. 4(b)) corresponds to a reversal of the flow direction (note that $|U_{cl}|$ is plotted in Fig. 4(b)).

To understand the relationship between the irreversible flow behaviour depicted in Fig. 4(b) and the rate at which the material is loaded/unloaded (the time t_0 per step used in the controlled stress pressure ramp), we have studied controlled pressure ramps for various values of t_0, Fig. 5. For clarity reasons, in Fig. 5(a) we present the results obtained for increasing pressures and in Fig. 5(b) those obtained for decreasing pressures. The data sets are colour coded (see the top color bars) according to the value of time per pressure step t_0. For both increasing and decreasing pressure drops, a significant dependence on the time per step is observed. For reference, we added to the increasing pressure branch data presented in Fig. 5(a) the steady-state results obtained from the creep tests presented in Fig. 2 as open red diamonds.

On the increasing branch of the pressure ramp (Fig. 5(a)) the data points merge with the steady state velocity values at large imposed pressure drops. The value of the pressure drop where the unsteady data merge, however, depends systematically on the time per pressure step. For small values of t_0 (fast loading), the apparent yielding pressure is large but, as t_0 increases, it decreases monotonically towards the steady state value $\Delta P_c = 4$ (or

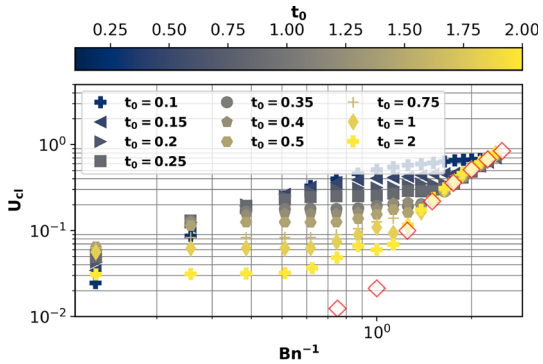

(a)

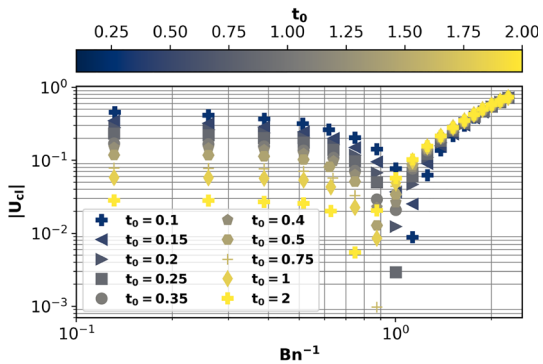

(b)

Fig. 5 (a) Dependence of the centre line velocity U_{cl} on the inverse Bingham number Bn^{-1} computed on the increasing branch of pressure ramps for several values of the time per step t_0. The empty red diamonds are values computed via creep tests (see Fig. 2)(b) Dependence of the center line velocity $|U_{cl}|$ on the inverse Bingham number Bn^{-1} computed on the decreasing branch of pressure ramps for several values of the time per step t_0

$Bn_c = 1$). This indicates that the apparent stress at which the material starts to yield near the walls depends on the characteristic rate at which the material is loaded.

Prior to yielding, the center-line velocities align on a plateau qualitatively similar to the plateau observed during the increasing/decreasing controlled stress ramps performed in a plate-plate rheometric setup, [9,13]. Through these rheological studies, the plateau value is related to the elastic modulus of the solid phase (see, for example, Fig. 12 and the discussion in Sec. 3.4 of [13]). For each value of the time per pressure value, the measurements of $|U_{cl}|$ performed on the unloading branch of the pressure ramp exhibit a cusp related to an elastic-recoil effect manifested through a reversal of the flow direction, Fig. 5(b). Such flow reversal effect has been observed experimentally, [11]. Regardless of the value of t_0, the flow reversal event is observed at a pressure drop corresponding to the steady state yielding, $\Delta P_c \approx 4$ ($Bn_c \approx 1$). Corresponding to the terminal stages of the unloading process when the imposed pressures become smaller than ΔP_c, the velocity data align on plateaus. These plateau values decrease monotonically with increasing value of the time per step t_0 which is fully consistent with the experimental observations performed in a plate-plate rheometric setup (see Fig. 12b in Ref. [13]).

It is interesting to understand the quantitative relationship between the hysteresis of the flow states observed upon increasing/decreasing pressure drops and the characteristic time per step t_0 of the loading/unloading process.

For this purpose we have studied controlled pressure ramps for various values of the time per step t_0 and computed the area of the hysteresis $A = \int U_{cl}^{up} d\Delta P_{up} - \int |U_{cl}^{down}| d\Delta P_{down}$. The dependence of the hysteresis area on the time per step is shown in Fig. 6. Prior to reaching a steady state plateau corresponding to large values of t_0, the hysteresis area decays as a power law, $A \propto t_0^{-\alpha}$ with $\alpha \approx 0.34$. This power law scaling is consistent with the experimental observations performed in a unsteady pipe flow, [11], but the experimental value of the scaling exponent was found roughly three times smaller, $\alpha \approx 0.1$. A possible reason for this discrepancy

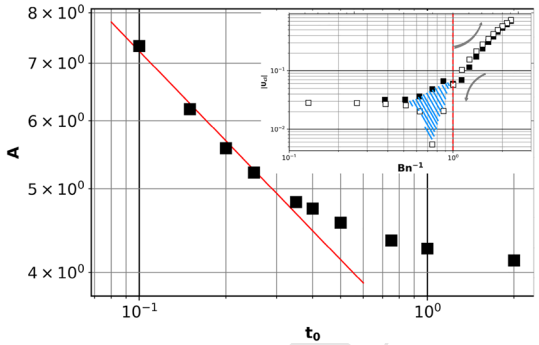

Fig. 6 Dependence of the hysteresis area A on the time per pressure step t_0. The solid line is a power law fitting function, $A = 3.25 \cdot t_0^{-0.34}$. A hysteresis loop is exemplified in the inset

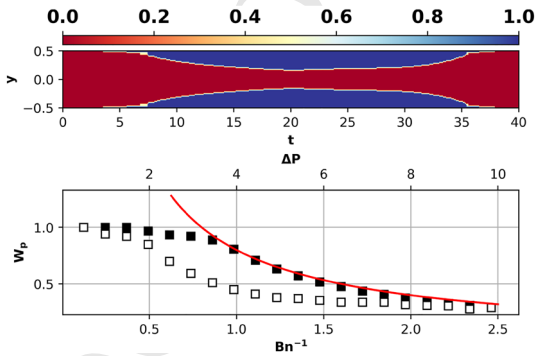

Fig. 7 **Top**: Space-time diagram of yielded/unyielded flow regions **Bottom**: Dependence of the width of the unyielded plug on the inverse Bingham number. The full/empty symbols refer to the increasing/decreasing branches of the ramp. The solid line is a guide for the eye, $W_p \propto Bn$

may relate to the presence of wall slip during the pipe flow experiments and the three dimensionality of the experimental flow channel. This result is also consistent with the scaling behavior of the magnitude of the rheological hysteresis observed during tests performed with Carbopol gels in a plate-plate geometry but the scaling exponent is once more different, $\alpha \approx 0.64$, [9]. For $t_0 > 1$, the hysteresis area seems to approach a plateau. This particular value of the time per step may be understood as a crude estimate of the polymeric relaxation time.

The irreversible flow behavior observed upon increasing/decreasing pressure drops equally manifests in the dynamics of the yielded/uni-yielded regions. To make this point, we present in Fig. 7 (bottom) the dependence of the width of the plug W_p on the inverse Bingham number. A space-time diagram of the extent of yielded/unyielded regions is shown in the top panel.

Upon increasing pressure drops past the critical pressure ΔP_c, a gradual decrease of the plug width is observed (the full symbols in Fig. 7). Within the fully yielded flow regime, $\Delta P > \Delta P_c$, the plug width scales as $W_p \propto Bn$ in agreement with the analytical result for a Herschel-Bulkley fluid, [28]. When the pressure drop is decreased, a clear hysteresis related to a delayed re-formation of the solid regions is observed, the empty symbols in Fig. 7. On this branch of the ramp, the plug width no longer follows the power law scaling observed on the increasing pressure branch. It is interesting to note that, unlike the centerline velocities which overlap rather well above the yield point ΔP_c, the plug width is systematically smaller during the unloading branch than during the loading branch. It is instructive to explore the dynamics of the elastic stresses during the loading/unloading sequence. For this purpose, we illustrate in Fig. 8 calculations of the first normal stress difference N_1 averaged over the width of the channel and per time step during a loading/unloading process. On the top panel we present the space-time diagram of N_1.

Upon increasing the pressure drop along the increasing branch of the ramp, the first normal stress difference starts to increase monotonically past the critical yielding pressure P_c, the full symbols in Fig. 8. Along the decreasing branch of the ramp, the normal force difference does not drop back to zero indicating that the elastic stresses persist during the unloading process. As visible in the space-time diagram, the elastic stresses persist

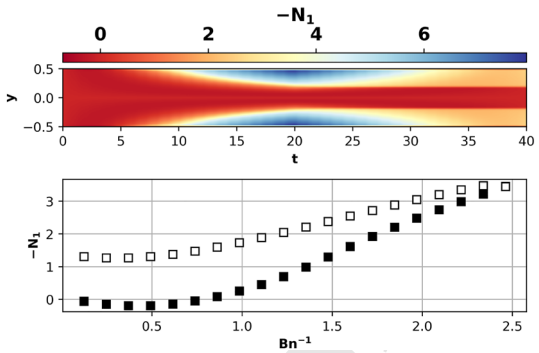

Fig. 8 **Top**: Space-time diagram of the first normal stress difference **Bottom**: Dependence of the first normal stress difference averaged over the channel width and per stress step on the Bingham number. The full/empty symbols refer to the increasing/decreasing branches of the ramp

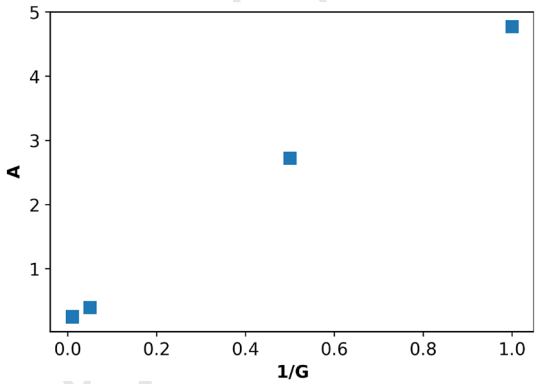

Fig. 9 Dependence of the hysteresis area A on the inverse elastic modulus $1/G$

in the vicinity of the solid boundaries of the channel. This result corroborates well with the strong hysteresis of the un-yielded plug and the delayed re-solidification observed during the unloading process illustrated in Fig. 7 and previously discussed.

To gain even further insights into the emergence of the flow hysteresis, we have studied controlled pressure drop increasing/decreasing ramps similar to that illustrated in Fig. 4 for a fixed value of the time per step $t_0 = 0.2$ and several values of the elastic modulus. The results of these simulations are summarized in Fig. 9.

The magnitude of the flow hysteresis is found to increase linearly with the magnitude of the elastic effects quantified by the inverse elastic modulus. A non-zero area of the hysteresis persists even in the limit of vanishingly small elastic effects because, even in the absence of elasticity, the loading/unloading process is characterized by finite time transient effects. The data presented in Fig. 9 clearly associate the observation of the flow hysteresis with the elastic effects.

3.3 Large amplitude oscillatory flows

Large amplitude oscillatory shear ($LAOS$) tests are instrumental in exploring the rich phenomenology of the dynamic yielding of yield stress materials in rheometric flows, [29–31].

During a $LAOS$ test, a harmonic forcing is imposed onto the material and its dynamic yielding is assessed by monitoring its response. Here we impose an oscillatory pressure drop $\Delta P = P_m \sin(\omega t)$ and, as in the case of the creep tests discussed in Sec. 3.1, we monitor the center-line axial velocity U. The ratio between the relaxation time of the material λ and the time scale associated to the harmonic forcing $t_f = 2\pi\omega^{-1}$ defines the Deborah number, $De = \lambda\omega$.

A visually convenient way of monitoring the response of the material to the oscillatory forcing is through the so called Lissajoux-Bowditch figures which are parametric representations of the transient forcing $\Delta P(t)$ on one axis and the response $U(t)$ on the other. The shape of the Lissajoux-Bowditch figure encodes key

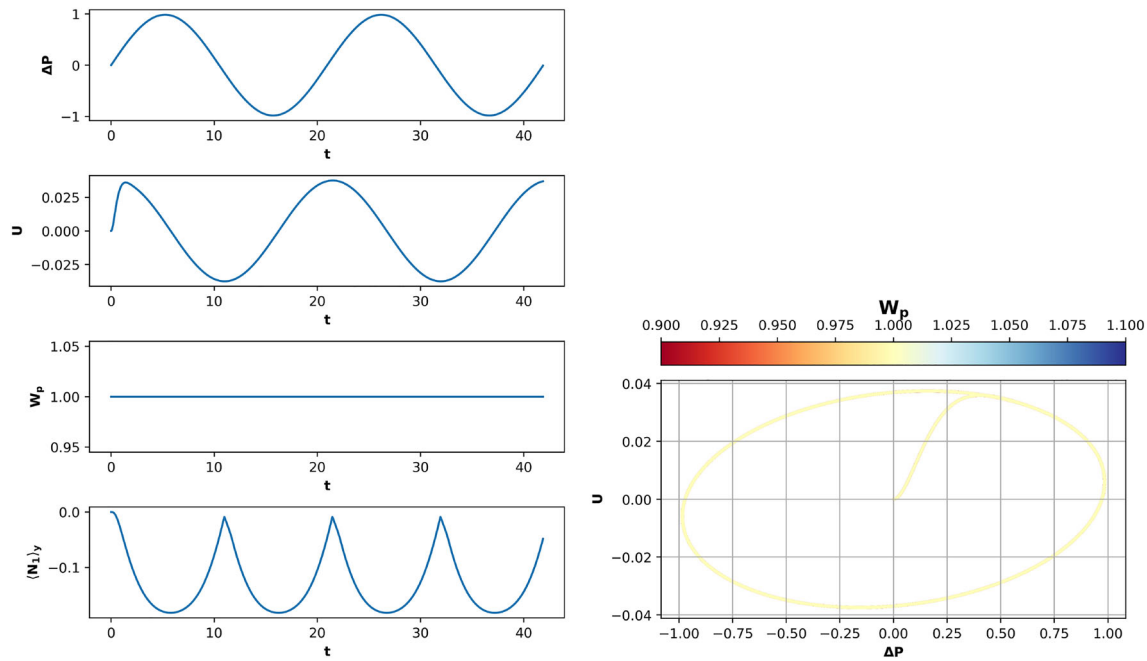

(a) (b)

Fig. 10 Results of oscillation tests performed with $\Delta P_{max} = 1$ and $De = 0.3$: (a) time series of several relevant quantities (b) corresponding Lissajoux-Bowditch curve

features of the response of the material forced with an amplitude P_m and a time scale set by the frequency ω. Such features include the degree of nonlinearity of the deformation process and the balance between energy storage and dissipation during the deformation process.

For LAOS tests performed in rheometric flows, the Lissajoux-Bowditch figures may be represented in two distinct set of coordinates [32]: (stress, strain) or (stress, strain-rate). The first choice is referred to as the *"elastic representation"* while the second as the *"viscous representation"*.

The choice $(\Delta P, U)$ of coordinates to describe the oscillatory process (which is natural for a pressure driven channel flow) is phenomenologically similar to the stress - rate of deformation representation or the viscous representation used to describe oscillatory rheological tests.

We exemplify oscillatory tests performed with $P_m = 1$ and $\omega = 0.3$ ($De = 0.3$) in Fig. 10. As the chosen pressure amplitude is smaller than the critical pressure drop $\Delta P_c = 4$ corresponding to the yielding, the response of the material is consistent with a linear elastic-solid behavior, Fig. 10(a). The material remains unyielded over the entire channel width ($W_p = 1$) and the subsequent loading/unloading results in an harmonic variation of the first normal stress difference. The corresponding Lissajoux-Bowditch curve has an elliptical shape, Fig. 10(b).

A substantially different behavior is observed for a pressure amplitude slightly larger than the critical yielding pressure $P_m = 5$ and same Deborah number, Fig. 11. The time series of the centre-line velocity now exhibits strongly nonlinear features and the material partially yields during the forcing cycle, Fig. 11(a).

It is interesting to monitor the evolution of the Lissajoux-Bowditch curves with either increasing pressure amplitude at constant Deborah number or increasing Deborah number at constant pressure amplitude, Fig. 12.

When the amplitude of the pressure drop is increased past the critical yielding value $\Delta P_c = 4$ at a constant Deborah number, the Lissajoux-Bowditch figures evolve from an elliptical shape corresponding to an elastic deformation to a strongly elongated shape, Fig. 12(a). It is interesting to point out the self-intersection of the Lissajoux-Bowditch figure observed for the largest pressure drop amplitude explored ($P_m = 20$). Such effect has already been observed during $LAOS$ measurements performed in rheometric flows in a highly nonlinear regime of deformation when the data are presented in the stress-rate of strain coordinates. This self-intersection event has been attributed to an elastic overshoot effect when the stress is unloaded more quickly than the new deformation is accumulated, [33]. We believe that our observation is phenomenologically similar. At a fixed pressure amplitude $P_m = 5$ right above the yield point, the eccentricity of the Lissajoux-Bowditch

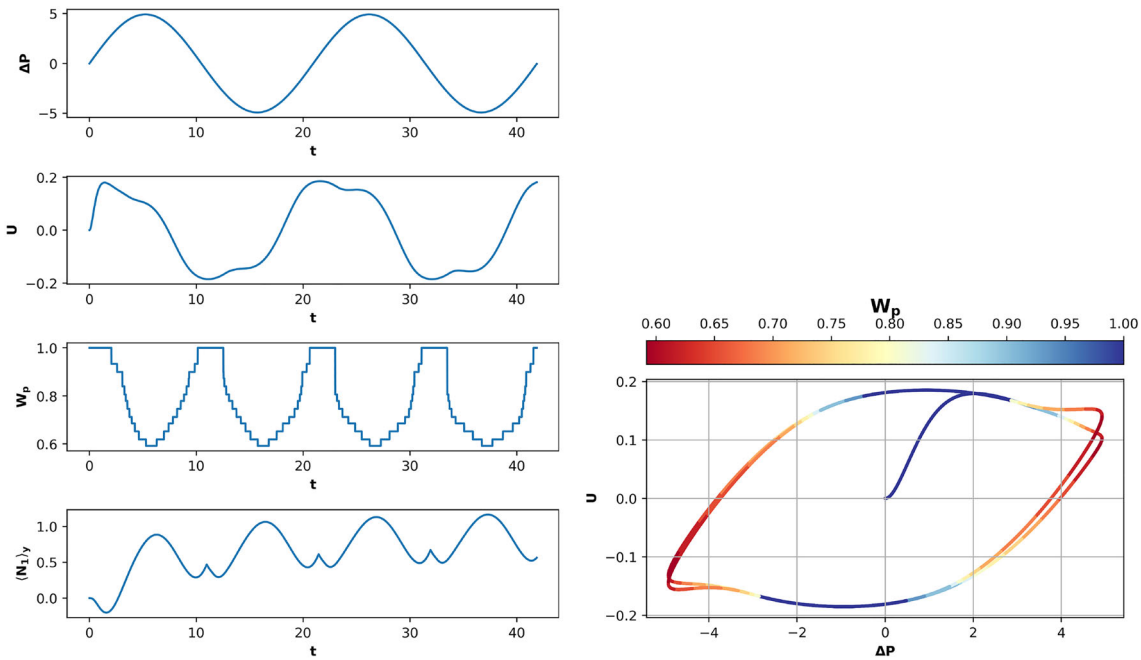

(a) (b)

Fig. 11 Results of oscillation tests performed with $P_m = 5$ and $De = 0.3$: (a) time series of several relevant quantities (b) corresponding Lissajoux-Bowditch curve. The color refers to the magnitude of the unyielded plug W_p

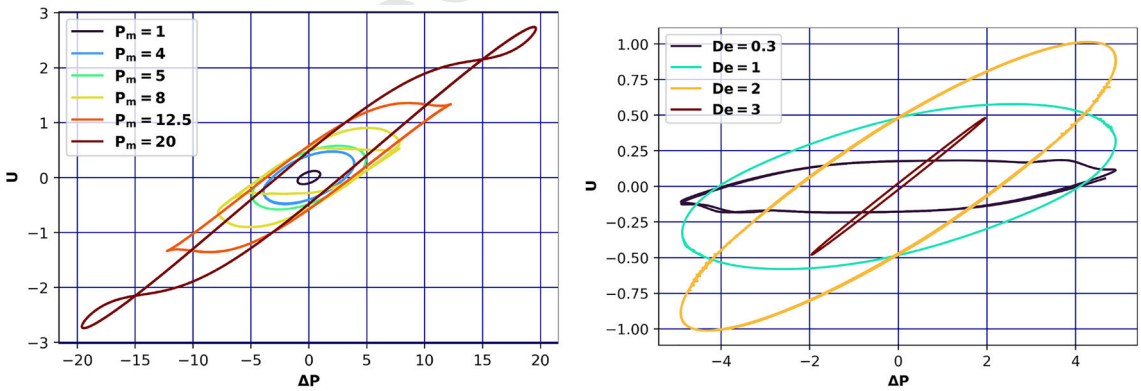

(a) (b)

Fig. 12 Lissajoux-Bowditch figures obtained at a fixed $De = 1$ and various amplitudes of the pressure drop P_m indicated in the insert. Lissajoux-Bowditch figures obtained for a fixed amplitude of the pressure drop $P_m = 5$ and various values of the Deborah number De indicated in the insert

curves increases gradually as the Deborah number is progressively increased, Fig. 12(b). The shape of the Lissajoux-Bowditch curve provides a crude indicator of the dominant deformation regime.

A partial re-construction of the Pipkin space which consists of Lissajoux-Bowditch curves obtained for several forcing amplitudes P_m and Deborah numbers [34] is presented in Fig. 13. For small amplitudes of the pressure drop, the Lissajoux-Bowditch curves are elliptic which implies an approximately linear viscoelastic response of the material. As the pressure drop amplitude is gradually increased at a constant Deborah number, signatures of nonlinear deformation emerge in the form of cusp points and self intersections of the Lissajoux-Bowditch figures.

The area of a Lissajoux-Bowditch curve $\mathscr{P}_d = \oint U\,dP$ represents the deformation power stored/dissipated during one forcing cycle. The dissipated power $\mathscr{P}_d$ depends on both the pressure drop amplitude P_m and the Deborah number De, Fig. 14. At a fixed Deborah number the dissipated power $\mathscr{P}_d$ increases with increasing

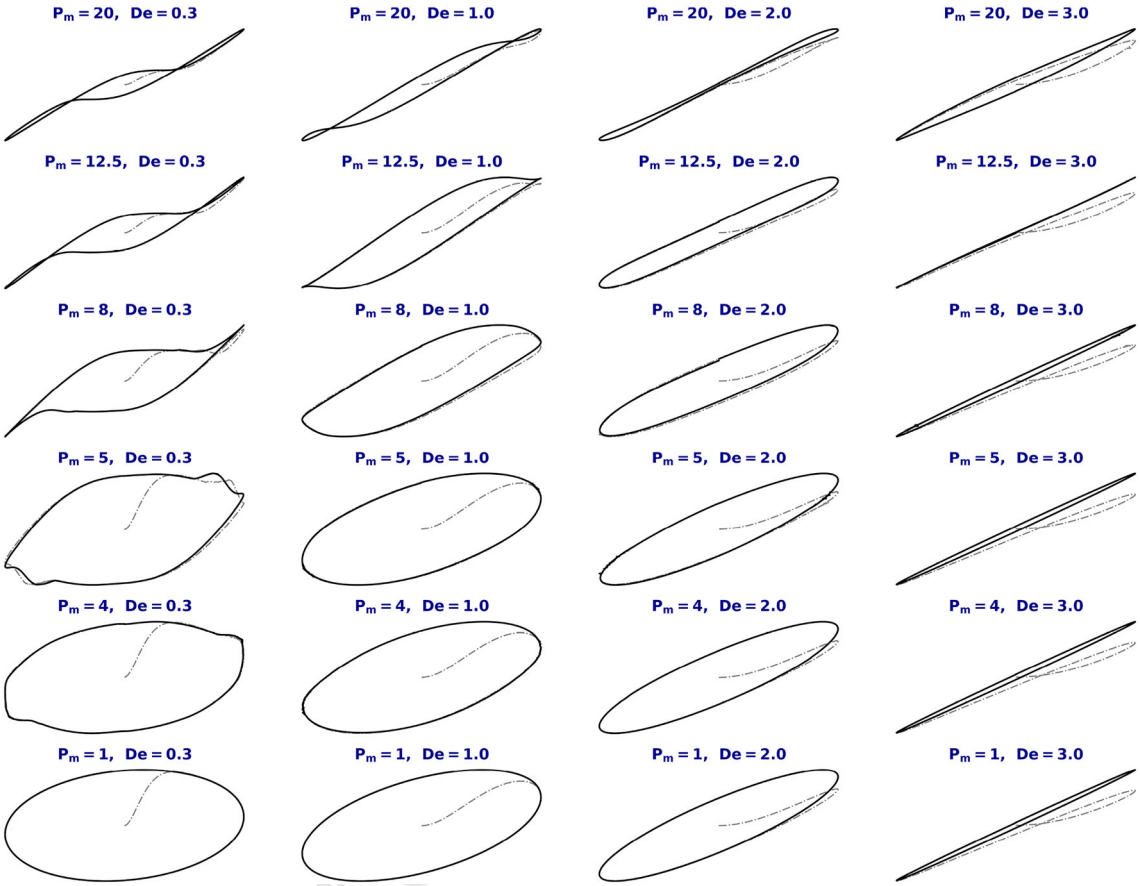

Fig. 13 Partial reconstruction of the Pipkin space. The pressure amplitudes and the Deborah numbers corresponding to each Lissajoux-Bowditch curve are indicated in the top inserts. For visual clarity, the Lissajoux-Bowditch curves are plotted on normalized coordinates

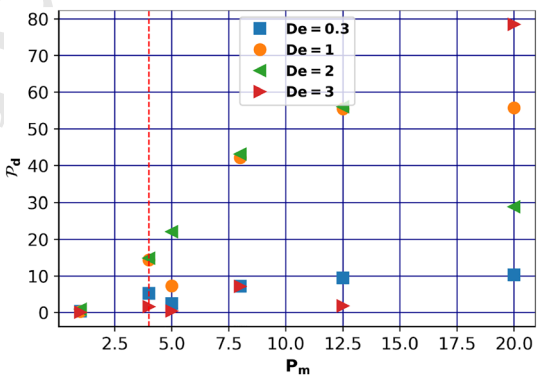

Fig. 14 Dependence of the power dissipated per forcing cycle $\mathscr{P}_d$ on the pressure amplitude P_m for several Deborah numbers detailed in the figure insert. The vertical dashed line marks the critical yielding pressure $P_m^c = 4$

amplitude of the pressure drop. For each Deborah number, the solid fluid transition is clearly visible at $P_m = \Delta P_c = 4$, the vertical dashed line in Fig. 14. Bellow the yield point the power is dissipated via plastic and elastic effects. As P_m is gradually increased past the yield point, the viscous dissipation becomes increasingly relevant.

4 Conclusions, discussion, outlook

A systematic numerical investigation of transient behavior of pressure driven flows of a elasto-viscoplastic material in a plane channel is presented. The response of the material to external stress is modeled by the Herschel-Bulkley variant of the Saramito constitutive model [17]. This model combines yield stress and viscoelastic behaviors. Unlike microstructural lumped models that are mostly suitable to describe the elastoviscoplastic behavior in rheometric flows (see for example the model proposed by [9] and similar models referred to therein), the tensorial nature of the SRM model involving the upper convective derivative makes it an attractive choice for describing non-rheometric flows of elasto-viscoplastic materials.

Through this manuscript we are testing the ability of the SRM-HB model to describe non-stationary flows of a elasto-viscoplastic material in a plane channel flow configuration. The transient dynamics of the yielding process are studied for three distinct types of forcing: creep tests performed for constant imposed pressure drops, Sec. 3.1, unsteady increasing/decreasing pressure drop ramps, 3.2 and, finally, large amplitude oscillatory (LAOS) tests Sec. 3.3.

During creep flows performed at a constant imposed pressure drop ΔP a permanent flow can be established only if the imposed pressure drop exceeds a critical value, $\Delta P \geq \Delta P_c$, Fig. 2. Regardless the value of the imposed pressure drop an overshoot behavior manifested through the emergence of a local maximum of the transient axial velocity is observed, Fig. 3(a). Prior to the overshoot, the material is un-yielded over the entire width of the channel - see panels (1-2) in Fig. 3(b). Yet, unlike in the case of a Herschel-Bulkley material, the un-yielded velocity profiles are not flat which indicates that the material behaves as an elastic solid in its un-yielded state. Right after the overshoot is observed, the material starts to gradually yield in the proximity of the channel walls, panel (3) in Fig. 3(b). At longer time instants, a steady state is reached and a flat central plug consistent with a Herschel-Bulkley behavior forms - panel (4) in Fig. 3(b).

The flow states observed upon increasing/decreasing linear ramps in the pressure drop Fig. 4(a) are generally irreversible and a rheological hysteresis is systematically observed, Fig. 4(b). The yielding process observed during controlled stress ramps is gradual. Corresponding to low imposed pressure drops, the center line velocity exhibits a plateau indicating an elastic solid behavior along both branches of the ramp. For pressure drops larger than the yielding value $\Delta P_c = 4$, the two branches of the ramp merge and the reversibility of the flow states is fully restored.

A first factor that controls the magnitude of the flow irreversibility (or rheological hysteresis) relates to the characteristic time t_0 per step of the controlled pressure drop ramp. Except for the range $\Delta P \geq \Delta P_c$, the dependence of the center line velocity on the imposed pressure drop depends systematically on the time per step t_0, Fig. 5. The area of the hysteresis observed during the loading/unloading process scales as a power law, $A \propto t_0^{-0.34}$ Fig. 6. This scaling result is in fair agreement with measurements performed with Carbopol gels unsteadily driven in a circular pipe [11]. Together with the hysteresis of the center-line velocity, one observes a hysteresis of the plug width upon increasing/decreasing pressure drops, Fig. 7.

As indicated by the large hysteresis of the first normal stress difference observed upon the loading/unloading sequence Fig. 8, the second factor controlling the magnitude of the hysteresis of flow states relates to the elasticity. In rheometric settings, the emergence of rheological hysteresis of deformation states of pasty materials is generally attributed to several factors which often manifest in a coupled manner: elasticity [35,36], thixotropy/anti-thixotropy [36], shear banding [37]. Unlike through experimental studies where various potential sources of the hysteresis behavior can not be easily separated, through this numerical study using the SRM-HB model we deal with only one potential source: the elasticity of the material. Thus, in the present case the hysteresis of the deformation states appears to solely originate from the elastic effects. This is corroborated by the observation of a linear increase of the hysteresis area with the inverse elastic modulus, Fig. 9.

A third type of external forcing tested through this study is the oscillatory forcing where the flow is driven by imposing an oscillatory pressure drop. Such forcing closely mimics the $LAOS$ tests commonly employed through rheological tests in order to test the dynamic yielding process in a nonlinear regime of deformations. Such type of forcing is widely employed through rheological tests but, to our best knowledge, very little explored in non-rheometric settings such as the plane channel flow studied here. The flow response to the imposed oscillatory pressure drop depends on both the amplitude of the forcing and its frequency (or, the Deborah number), Figs. 10,11,12. The $LAOS$ tests are instrumental in studying the emergence of nonlinear effects during the transient yielding process which are manifested by the presence of cusp points and self-intersections of the Lissajoux-Bowditch curves. A comprehensive panorama of the response to oscillatory forcing is obtained by the partial reconstruction of the Pipkin space, Fig. 13.

To conclude, we have shown that the SRM-HB model accurately captures the transient dynamics of flows of elasto-viscoplastic materials by reproducing several important features observed in experiments performed with a Carbopol gel as an elasto-viscoplastic material, [11]: elastic overshoot, hysteresis of the flow states upon loading/unloading. Along a more practical line, this study suggests one may use simple non-rheometric unsteady flows to infere the key rheological parameters of an elasto-viscoplastic material. The yield stress may be inferred from both creep tests and linear ramps of the pressure drop by measurements of the critical yielding pressure drop ΔP_c, the consistency and the power law index may be inferred from measurements of the center-line velocity during pressure ramps (for $\Delta P > \Delta P_c$) and estimates of the relaxation time may be obtained from measurements of the hysteresis area versus the rate of loading. At this point, however, we believe that additional theroetical developments are needed in order to quantitatively interpret LAOS measurements in terms of material properties as it is currently done for LAOS measurements performed in rheometric flows.

Acknowledgements T.B. gratefully acknowledges the Erskine Foundation of the University of Canterbury for a one month fellowship. M. M-G. gratefully acknowledges the University of Nantes for a visiting fellowship.

Declarations

Author contributions The project was jointly designed by T. B. and M. M-G. The numerical simulations have been designed, implemented and conducted by T. B. The post processing of the numerical data was performed by T. B. The first draft of the paper was written by T. B. Both authors have contributed to improving the initial draft.

Data Availibility No datasets were generated or analysed during the current study.

Conflict of interest/Competing interests We hereby declare having no conflicts of interests.

Ethics approval Not applicable

Consent to participate Not applicable

Consent for publication Not applicable

Code availability Not applicable

Appendix A Semi-analytical solution for the steady flow

We derive here a semi-analytical solution for the steady plane channel flow driven at a constant imposed pressure drop ΔP following the derivation for the Bingham variant of the Saramito model presented in Ref. [38].

We solve over the domain: $y \in [-1/2, 1/2]$, with no-slip boundary conditions. Note that at $y = y^*$, the yield surface, we have $\frac{du}{dy} = 0$. The equations to solve are:

$$\frac{d\tau_{xy}}{dy} + \beta\frac{d^2u}{dy^2} = -\Delta P \tag{A1}$$

$$\frac{d\tau_{yy}}{dy} = 0 \tag{A2}$$

$$-2Wi\,\tau_{xy}\frac{du}{dy} + \left(\frac{|\boldsymbol{\tau}_p^d| - Bn}{|\boldsymbol{\tau}_p^d|^n}\right)_+^{1/n}\tau_{xx} = 0 \tag{A3}$$

$$-Wi\,\tau_{yy}\frac{du}{dy} + \left(\frac{|\boldsymbol{\tau}_p^d| - Bn}{|\boldsymbol{\tau}_p^d|^n}\right)_+^{1/n}\tau_{xy} = (1-\beta)\frac{du}{dy} \tag{A4}$$

$$\left(\frac{|\boldsymbol{\tau}_p^d| - Bn}{|\boldsymbol{\tau}_p^d|^n}\right)_+^{1/n}\tau_{yy} = 0. \tag{A5}$$

Here

$$\left(\frac{|\boldsymbol{\tau}_p^d| - Bn}{|\boldsymbol{\tau}_p^d|^n}\right)_+^{1/n} = \max\left(0, \left(\frac{|\boldsymbol{\tau}_p^d| - Bn}{|\boldsymbol{\tau}_p^d|^n}\right)^{1/n}\right). \tag{A6}$$

From from (A2) and (A5) it is clear that $\tau_{yy} = 0$.
Integrating (A1) once, we get

$$\tau_{xy} = -\Delta P y - \beta \frac{du}{dy}. \tag{A7}$$

This can be rearranged as

$$\frac{du}{dy} = \frac{-\tau_{xy} - \Delta P y}{\beta}. \tag{A8}$$

Solving first for the yielded region, we can use (A3) and (A5) to get an expression for τ_{xy},

$$\left(\frac{|\boldsymbol{\tau}_p^d| - Bn}{|\boldsymbol{\tau}_p^d|^n}\right)^{1/n} \tau_{xy} = (1-\beta)\frac{du}{dy}. \tag{A9}$$

Substituting (A9) into (A4):

$$-2Wi\left(\frac{|\boldsymbol{\tau}_p^d| - Bn}{|\boldsymbol{\tau}_p^d|^n}\right)^{1/n} \tau_{xy}^2 + \left(\frac{|\boldsymbol{\tau}_p^d| - Bn}{|\boldsymbol{\tau}_p^d|^n}\right)^{1/n} (1-\beta)\tau_{xx} = 0. \tag{A10}$$

Now we can express τ_{xx} in terms of τ_{xy}

$$\tau_{xx} = \frac{2Wi}{1-\beta}\tau_{xy}^2. \tag{A11}$$

Substituting into $|\boldsymbol{\tau}_p^d|$ we get,

$$|\boldsymbol{\tau}_p^d| = \sqrt{\tau_{xy}^2 + \frac{\tau_{xx}^2}{4}} = \sqrt{\tau_{xy}^2 + \frac{Wi^2\tau_{xy}^4}{(1-\beta)^2}}. \tag{A12}$$

Hence, using (A9) in (A8) we have an expression for τ_{xy}:

$$\left(\frac{|\boldsymbol{\tau}_p^d| - Bn}{|\boldsymbol{\tau}_p^d|^n}\right)^{1/n} \tau_{xy} = \frac{\beta - 1}{\beta}\left(\Delta P y + \tau_{xy}\right). \tag{A13}$$

We can use a root-finding method to solve (A13) and obtain $\tau_{xy}(y)$ in the yielded regions.
It is not difficult to calculate that the yield surface is located at

$$y^* = \pm\left(\frac{\sqrt{1 + \frac{4Wi^2Bn^2}{(1-\beta)^2}} - 1}{2Wi^2\frac{(\Delta P)^2}{(1-\beta)^2}}\right)^{1/2}. \tag{A14}$$

Appendix B Time step convergence

We focus on the dependence of the hysteresis loop result presented in Fig. 4(b) on the choice of the maximum time step DT of the simulation.
The dependence of the absolute value of the center line velocity $|U_{cl}|$ on the driving pressure drop ΔP obtained during an increasing/decreasing ramp (see Fig. 4) obtained for several values of the maximal time per step DT ranging in between $5 \cdot 10^{-6}$ and $2 \cdot 10^{-5}$ are shown in Fig. 15. It is rather clear from this figure that the results obtained with four distinct choices of the maximal time step perfectly overlap.

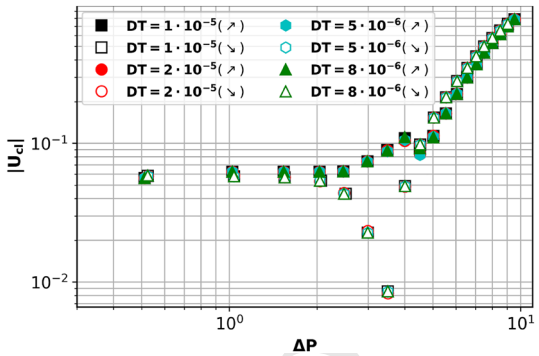

Fig. 15 Center line velocity U_{cl} computed during a pressure ramp for various choices of the time per step DT indicated in the insert. All calculations used the same adaptive grid. The full/empty symbols refer to the increasing/decreasing branches of the ramp. The time per pressure drop step was was $t_0 = 1$

Appendix C Additional grid convergence tests

The grid independence tests discussed in Sec. 2.2 and illustrated in Fig. 1(a) refer to a steady state flow. Yet, a number of important results obtained through this study refer to unsteady flows. It is therefore important to prove the grid independence for unsteady flows.

A first unsteady flow case chosen to test the grid independence relates to the creep tests already analyzed in Sec. 3.1.

In Fig. 16 we illustrated time series of the center line velocity computed during a creep test computed for several choices of the base grid. Except for a very narrow time interval right after the overshoot is observed (see the inset in Fig. 16) the different data sets practically overlap which demonstrates the grid independence of the results.

A second unsteady flow case we chose to test the grid independence refers to the increasing/decreasing controlled pressure flow ramps discussed in detail in Sec. 3.2. Results of the hysteresis of the flow states computed during a pressure ramp with several choices of the grid are exemplified in Fig. 17. A quick visual inspection of these three distinct numerical results plotted on a logarithmic scale indicates that the hysteresis result is practically independent on the choice of the grid.

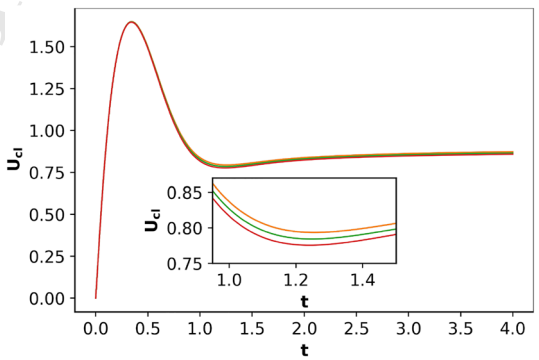

Fig. 16 Time series of the centerline speed obtained during a creep test with $\Delta P_0 = 10$ for several grid levels $\Delta y = 1/2^N$ with $N \in \{4, 5, 6, 7\}$. The inset shows a magnified view that highlights minor differences between the tests

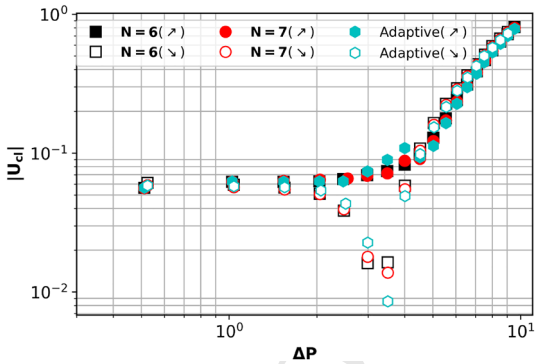

Fig. 17 Center line velocity U_{cl} computed during a pressure ramp for several choices of the grid indicated in the insert. The full/empty symbols refer to the increasing/decreasing branches of the ramp. The time per pressure drop step was $t_0 = 1$ and the maximal time step during computations is $DT = 10^{-5}$

References

1. Saramito, P.: A new elastoviscoplastic model based on the herschel–bulkley viscoplastic model. J. Non-Newton. Fluid Mech. **158**(1), 154–161 (2009). https://doi.org/10.1016/j.jnnfm.2008.12.001. (**Visco-plastic fluids: From theory to application**)
2. Barnes, H.A., Walters, K.: The yield stress myth? Rheol. Acta **24**, 323–326 (1985)
3. Barnes, H.A.: The yield stress-a review or '$\pi\alpha\nu\tau\alpha\rho\epsilon\iota$'-everything flows? J. Non-Newton. Fluid Mech. **81**(1–2), 133–178 (1999)
4. Ovarlez, G., Cohen-Addad, S., Krishan, K., Goyon, J., Coussot, P.: On the existence of a simple yield stress fluid behavior. J. Non-Newton. Fluid Mech. **193**, 68–79 (2013). https://doi.org/10.1016/j.jnnfm.2012.06.009. (**Viscoplastic Fluids: From Theory to Application**)
5. Moller, P.C.F., Fall, A., Bonn, D.: Origin of apparent viscosity in yield stress fluids below yielding. EPL (Europhysics Letters) **87**(3), 38004 (2009)
6. Jaworski, Z., Spychaj, T., Story, A., Story, G.: Carbomer microgels as model yield-stress fluids. Rev. Chem. Eng. **38**(7), 881–919 (2022). https://doi.org/10.1515/revce-2020-0016
7. Curran, S.J., Hayes, R.E., Afacan, A., Williams, M.C., Tanguy, P.A.: Properties of carbopol solutions as models for yield-stress fluids. J. Food Sci. **67**(1), 176–180 (2002). https://doi.org/10.1111/j.1365-2621.2002.tb11379.x
8. Piau, J.M.: Carbopol gels: elastoviscoplastic and slippery glasses made of individual swollen sponges: Meso- and macroscopic properties, constitutive equations and scaling laws. J. Non-Newton. Fluid Mech. **144**(1), 1–29 (2007). https://doi.org/10.1016/j.jnnfm.2007.02.011
9. Putz, A.M.V., Burghelea, T.I.: The solid-fluid transition in a yield stress shear thinning physical gel. Rheol. Acta **48**, 673–689 (2009)
10. Divoux, T., Grenard, V., Manneville, S.: Rheological hysteresis in soft glassy materials. Phys. Rev. Lett. **110**, 018304 (2013). https://doi.org/10.1103/PhysRevLett.110.018304
11. Poumaere, A., Moyers-Gonzalez, M., Castelain, C., Burghelea, T.: Unsteady laminar flows of a carbopol gel in the presence of wall slip. J. Non-Newton. Fluid Mech. **205**, 28–40 (2014). https://doi.org/10.1016/j.jnnfm.2014.01.003
12. Kebiche, Z., Castelain, C., Burghelea, T.: Experimental investigation of the rayleigh-bénard convection in a yield stress fluid. J. Non-Newton. Fluid Mech. **203**, 9–23 (2014). https://doi.org/10.1016/j.jnnfm.2013.10.005
13. Younes, E., Himl, M., Stary, Z., Bertola, V., Burghelea, T.: On the elusive nature of carbopol gels: "model", weakly thixotropic, or time-dependent viscoplastic materials? J. Non-Newton. Fluid Mech. **281**, 104315 (2020). https://doi.org/10.1016/j.jnnfm.2020.104315
14. Gonzalez, M.M., Burghelea, T., Mak, J.: Linear stability analysis for plane-poiseuille flow of an elastoviscoplastic fluid with internal microstructure for large reynolds numbers. J. Non-Newton. Fluid Mech. **166**(9–10), 515–531 (2011)
15. Moyers-González, M., Castelain, C., Burghelea, T.: Numerical study of unsteady pipe flow of an elastoviscoplastic fluid. J. Non-Newton. Fluid Mech. **309**, 104898 (2022). https://doi.org/10.1016/j.jnnfm.2022.104898
16. Fraggedakis, D., Dimakopoulos, Y., Tsamopoulos, J.: Yielding the yield stress analysis: A thorough comparison of recently proposed elasto-visco-plastic (evp) fluid models. J. Non-Newton. Fluid Mech. **236**, 104–122 (2016). https://doi.org/10.1016/j.jnnfm.2016.09.001
17. Saramito, P.: A new constitutive equation for elastoviscoplastic fluid flows. J. Non-Newton. Fluid Mech. **145**(1), 1–14 (2007). https://doi.org/10.1016/j.jnnfm.2007.04.004
18. Park, Y.S., Liu, P.L.-F.: Oscillatory pipe flows of a yield-stress fluid. J. Fluid Mech. **658**, 211–228 (2010)
19. Belblidia, F., Tamaddon-Jahromi, H.R., Webster, M.F., Walters, K.: Computations with viscoplastic and viscoelastoplastic fluids. Rheol. Acta **50**, 343–360 (2011)
20. Fraggedakis, D., Dimakopoulos, Y., Tsamopoulos, J.: Yielding the yield-stress analysis: a study focused on the effects of elasticity on the settling of a single spherical particle in simple yield-stress fluids. Soft Matter **12**, 5378–5401 (2016). https://doi.org/10.1039/C6SM00480F
21. Moschopoulos, P., Spyridakis, A., Varchanis, S., Dimakopoulos, Y., Tsamopoulos, J.: The concept of elasto-visco-plasticity and its application to a bubble rising in yield stress fluids. J. Non-Newton. Fluid Mech. **297**, 104670 (2021). https://doi.org/10.1016/j.jnnfm.2021.104670

22. Kordalis, A., Dimakopoulos, Y., Tsamopoulos, J.: Hydrodynamic interaction between coaxially rising bubbles in elasto-visco-plastic materials: Bubbles with a wide range of relative sizes. Phys. Rev. Fluids **9**, 093301 (2024). https://doi.org/10.1103/PhysRevFluids.9.093301
23. Parvar, S., Chaparian, E., Tammisola, O.: General hydrodynamic features of elastoviscoplastic fluid flows through randomised porous media. Theoret. Comput. Fluid Dyn. **38**(4), 531–544 (2024). https://doi.org/10.1007/s00162-024-00705-1
24. Oldroyd, J.G., Wilson, A.H.: On the formulation of rheological equations of state. Proceedings of the Royal Society of London. Series A. Mathematical and Physical Sciences **200**(1063), 523–541 (1950). https://doi.org/10.1098/rspa.1950.0035
25. Bird, R.B., Hassager, O., Armstrong, R.C., Curtiss, C.F.: Dynamics of Polymeric Liquids, vol. 1. Wiley, New York (1977)
26. Popinet, S., Collaborators basilisk.fr. [Accessed 02-01-2025] ([Accessed 02-01-2025])
27. López-Herrera, J.M., Popinet, S., Castrejón-Pita, A.A.: An adaptive solver for viscoelastic incompressible two-phase problems applied to the study of the splashing of weakly viscoelastic droplets. J. Non-Newton. Fluid Mech. **264**, 144–158 (2019). https://doi.org/10.1016/j.jnnfm.2018.10.012
28. Coussot, P.: Rheometry of Pastes. Suspensions and Granular Materials, John Willey & Sons, New Jersey (2005)
29. Ewoldt, R.H., Hosoi, A.E., McKinley, G.H.: New measures for characterizing nonlinear viscoelasticity in large amplitude oscillatory shear. J. Rheol. **52**(6), 1427–1458 (2008). https://doi.org/10.1122/1.2970095
30. Dimitriou, C.J., Ewoldt, R.H., McKinley, G.H.: Describing and prescribing the constitutive response of yield stress fluids using large amplitude oscillatory shear stress (LAOStress). J. Rheol. **57**(1), 27–70 (2013). https://doi.org/10.1122/1.4754023
31. Kamani, K., Donley, G.J., Rogers, S.A.: Unification of the rheological physics of yield stress fluids. Phys. Rev. Lett. **126**, 218002 (2021). https://doi.org/10.1103/PhysRevLett.126.218002
32. Ewoldt, R.H.: Nonlinear Viscoelastic Materials: Bioinspired Applications and New Characterization Measures, (2009)
33. Ewoldt, R.H., McKinley, G.H.: On secondary loops in laos via self-intersection of lissajous–bowditch curves. Rheol. Acta **49**(2), 213–219 (2009). https://doi.org/10.1007/s00397-009-0408-2
34. Pipkin, A.C.: Lectures on Viscoelasticity Theory. Springer, New York (1986)
35. Sharma, S., Shankar, V., Joshi, Y.M.: Viscoelasticity and rheological hysteresis. J. Rheol. **67**(1), 139–155 (2023). https://doi.org/10.1122/8.0000462
36. Wang, Y., Ewoldt, R.H.: Thixotropy, antithixotropy, and viscoelasticity in hysteresis. J. Rheol. **67**(6), 1199–1219 (2023). https://doi.org/10.1122/8.0000620
37. Divoux, T., Grenard, V., Manneville, S.: Rheological hysteresis in soft glassy materials. Phys. Rev. Lett. **110**, 018304 (2013). https://doi.org/10.1103/PhysRevLett.110.018304
38. Chaparian, E., Ardekani, M.N., Brandt, L., Tammisola, O.: Particle migration in channel flow of an elastoviscoplastic fluid. J. Non-Newton. Fluid Mech. **284**, 104376 (2020). https://doi.org/10.1016/j.jnnfm.2020.104376